Ultramicroscopy 218 (2020) 113086

Contents lists available at ScienceDirect

Ultramicroscopy

journal homepage: www.elsevier.com/locate/ultramic

Analyzing contrast in cryo-transmission electron microscopy: Comparison of electrostatic Zach phase plates and hole-free phase plates

Martin Obermair[a,*], Simon Hettler[b], Chyongere Hsieh[c], Manuel Dries[a], Michael Marko[c,d], Dagmar Gerthsen[a]

[a] Karlsruher Institut für Technologie (KIT), Laboratorium für Elektronenmikroskopie (LEM), Engesserstraße 7, 76131 Karlsruhe, Germany
[b] Universidad de Zaragoza, Instituto de Nanociencia de Aragón (INA), Laboratorio de Microscopías Avanzadas (LMA), C/ Mariano Esquillor s/n, Edificio I+D - Campus Río Ebro, 50018 Zaragoza, Spain
[c] New York State Department of Health (NYSDOH), Wadsworth Center, Empire State Plaza, P.O. Box 509, Albany, NY 12201-0509, United States
[d] College of Nanoscale Science and Engineering, SUNY Polytechnic Institute, 257 Fuller Road, Albany, NY 12203, United States

ARTICLE INFO

Keywords:
Cryo-transmission electron microscopy (TEM)
Phase plate
Phase contrast
Thin film
Biological specimen
Cryo-electron tomography (cryo-ET)

ABSTRACT

Phase plates (PPs) are beneficial devices to improve the phase contrast of life-science objects in cryo-transmission electron microscopy (TEM). The development of the hole-free (HF) PP, which consists of a thin carbon film, has led to impressive results due to its ease in fabrication, implementation and application. However, the phase shift of the HFPP can be controlled only indirectly. The electrostatic Zach PP uses a strongly localized and adjustable electrostatic potential to generate well-defined and variable phase shifts between scattered and unscattered electrons. However, artifacts in phase-contrast TEM images are induced by the presence of the PP rod in the diffraction plane. We present a detailed analysis and comparison of the contrast-enhancing capabilities of both PP types and their emerging artifacts. For this purpose, cryo-TEM images of a standard T4-bacteriophage test sample were acquired with both PP types. Simulated images reproduce the experimental images well and substantially contribute to the understanding of contrast formation. An electrostatic Zach PP was used in this work to acquire cryo-electron tomograms with enhanced contrast, which are of similar quality as tomograms obtained by HFPP TEM.

1. Introduction

The weak contrast of radiation-sensitive life-science objects in cryo-transmission electron microscopy (TEM) poses a fundamental physical limit to their structure determination. Also known as weak-phase objects (WPOs), life-science samples often consist of materials with low atomic number (e.g. water and carbon), which cause only a weak alteration of the incident electron wave. Thus, their structural features appear almost invisible in in-focus TEM images. A common way of increasing the contrast of WPOs is achieved by a defocusing of the objective lens, which leads, however, to the loss of resolution and image interpretability [1].

Physical phase plates (PPs) generate phase contrast by inducing a relative phase shift between the scattered and unscattered part of the electron wave in the back focal plane (BFP) of the objective lens, without the need to apply a strong defocus. Many PP designs have been developed [2] since the concept of phase-contrast imaging was first introduced for light microscopy in 1942 by Zernike [3] and later proposed for application in TEM by Boersch in 1947 [4]. PPs for TEM can be mainly subdivided into thin-film and electrostatic approaches. Zernike carbon-film-based PPs impose a phase shift on the scattered electrons that propagate through a thin amorphous carbon (aC) film, while the unscattered electrons remain unaffected because they propagate through a small microstructured hole in the center of the aC film [5]. The phase shift φ_{PP} depends on the mean inner potential V_0 of the PP material, the electron wavelength λ, the acceleration voltage U in volts (V) and the thickness of the aC film t and can be calculated from the following formula [6]:

$$\varphi_{PP} = \frac{\pi}{\lambda U} \cdot \frac{1 + 2\alpha U}{1 + \alpha U} \cdot V_0 \cdot t, \quad \alpha = 0.9788 \cdot 10^{-6} \frac{1}{V} \tag{1}$$

The film thickness of the Zernike PP is used to adjust the phase shift to $\pi/2$, which yields maximum phase contrast for WPOs. The radius of the Zernike-PP hole, which defines the cut-on frequency, limits the maximum periodicity or particle/object size that can be imaged with phase contrast. However, the quality of Zernike-PP-TEM images is

* Corresponding author.
E-mail address: martin.obermair@kit.edu (M. Obermair).

https://doi.org/10.1016/j.ultramic.2020.113086
Received 8 May 2020; Received in revised form 24 July 2020; Accepted 27 July 2020
Available online 29 July 2020

limited due to unavoidable fringing artifacts surrounding the imaged object, which are induced by the abrupt onset of the phase shift at the edge of the hole. Another drawback of Zernike PPs is irreversible deterioration of the aC film during irradiation with high-energy electrons, which results in electrostatic charging and affects the phase-shifting behavior. While the lifetime of the Zernike PP can be significantly increased if contamination is inhibited by heating the film to elevated temperatures [7], the regular replacement of an aC-film-based Zernike PP is unavoidable.

Electrostatic charging is a beneficial effect in the case of a hole-free (HF) PP, which is also referred to as a Volta PP [8,9]. A continuous aC film without an opening is positioned in the BFP of the objective lens, and the irradiation of the aC film with the intense zero-order beam (ZOB) creates a phase-shifting patch. This patch may be caused by either deposition of carbon contamination, being equivalent to positive charging [10], or by local modification of the aC film's electronic work function due to electron-stimulated desorption leading to negative charging [11]. The profile of the imposed phase shift is similar to the intensity profile of the ZOB but extends to higher spatial frequencies, especially in the case of negative charging [12]. Another beneficial effect is the gradual onset of the phase-shift profile, which leads to a substantial reduction of fringing effects. Moreover, the maximum object size for phase-contrast imaging is not strictly limited by a cut-on frequency. On the downside, the smooth-onset gradient of the phase profile produces a halo surrounding the imaged objects [8,12]. In comparison to the Zernike PP, which operates with a fixed phase shift, the exact phase shift of the HFPP is more difficult to control and depends on experimental parameters, such as the beam diameter, the irradiation time and the surface chemistry of the HFPP film. The phase shift can be roughly adjusted by the temperature of the aC film, which affects the surface chemistry and requires a heating device. Images with a moderate defocus can be used for quantitative determination of the phase shift by the position of the Thon rings [13]. HFPPs are commercially available and successfully used for single-particle reconstruction [14,15], tomographic reconstruction of proteins [16,17] and entire cells [18,19], as well as in solid-state physics [20]. However, there are some remaining difficulties to be solved. Especially in cryo-TEM, where most of the investigated life-science objects are radiation sensitive and endure only a low electron dose for imaging, the focus of the microscope has to be adjusted in an area some distance away from the region of interest. This is often realized by a shift of the electron beam (while avoiding any beam tilt) and requires a precise beam alignment so that the ZOB keeps its position on the phase-shifting patch [21]. Furthermore, a high degree of HFPP-holder stability is necessary to prevent drift of the phase-shift patch. Finally, the phase shift can only be adjusted indirectly and can vary. This is a drawback of the HFPP because a PP with an *in-situ* adjustable phase shift is desirable for more quantitative applications.

Electrostatic PPs satisfy the latter requirement because they use a tunable electrostatic field to shift the phase between the scattered and unscattered part of the electron wave. Until now, the most promising electrostatic PP is the Zach PP [22]. It is a microstructured device consisting of an aperture with a supporting rod extending towards the center of the aperture, which contains a shielded open electrode similar to an open-ended microcoaxial cable. By applying a voltage to the electrode, a strongly localized electrostatic potential builds up at the tip of the rod. By positioning it close to the ZOB, a phase shift is imposed on the unscattered electrons passing through the electrostatic field, while the scattered electrons remain unaffected. The phase shift can be controlled by the applied voltage and by the distance between the PP tip and the ZOB. The Zach-PP design, with its single supporting rod, minimizes the obstruction of spatial frequencies in the BFP. Its ability to enhance the phase contrast of different samples has been demonstrated [23,24]. Disadvantages of electrostatic Zach PPs are the elaborate fabrication procedure, the inhomogeneous phase-shift distribution, the blocking of spatial frequencies by the PP rod and sometimes an unwanted charge build-up on the PP structure.

T4 bacteriophages (T4s) were used as test objects in this work. They are excellent test samples to investigate phase contrast of life-science specimens by TEM because they contain features of different sizes. With a total length of ~250 nm, T4s consist of two major parts, a head and a tail. The head is a prolate icosahedron with a diameter of about 85 nm and a length of 115 nm [25]. The head consists of a 3-nm protein shell [26], the capsid, encapsulating the packaged deoxyribonucleic acid (DNA), the genome of the T4. The ~100-nm-long tail consists of a contractile tail sheath with a width of ~21 nm [26]. At one end of the tail, a hexagonal baseplate with 6 long tail fibers is attached. The contractile tail sheath appears in TEM images with a 4-nm periodicity due to its helical protein structure. When a T4 infects a bacterium, it settles down on the bacterial cell membrane, retracts the contractile tail sheath and penetrates the membrane with the tail tube to inject the DNA and infect the bacterium. In TEM specimens, T4s can be found in different stages of this infection cycle. Even though T4s are radiation sensitive, TEM imaging with an exposure up to ~140 $e^-/Å^2$ is possible without apparent sample degradation. Electron doses between 8 and 12 $e^-/Å^2$ per image applied in this work therefore allow to acquire TEM image series up to 17 images with negligible losses in image quality (a much lower dose per image is used for recording a tomographic tilt series).

We present in this work comparative cryo-TEM experiments conducted with the electrostatic Zach PP and with the HFPP to analyze contrast formation and evaluate artifacts. For this purpose, phase-contrast TEM imaging with Zach PPs and HFPPs was performed using plunge-frozen T4 samples. A detailed study of contrast enhancement is performed in experiment and by simulation. Simulations of Zach-PP- and HFPP-TEM images are in good agreement with experiments and provide a detailed understanding of the contrast of T4 features. We show that Zach-PP-TEM image formation is complex, with several contributing effects, while HFPP-TEM images can be understood by assuming a Lorentzian phase-shift profile. We also have performed cryo-electron tomography with Zach PPs for the first time and show results that compare well with tomography data from HFPP-TEM imaging.

2. Materials and methods

2.1. Samples and experimental procedures

The electrostatic Zach PPs used in this experiment consist of an objective aperture (diameter 100 μm) with a single supporting rod (width at the tip = 1 μm). The rod contains an open-ended Au electrode (height × width = 120 nm × 300 nm), which is surrounded by electrically insulating Si_3N_4 and Al_2O_3 layers (thicknesses 200 nm) and a surrounding shielding Au layer (thickness 120 nm). An additional aC coating (thickness 5 nm) over the Au layer minimizes electrostatic charging [23]. A strongly localized electrostatic field builds up at the tip of the Au electrode when a voltage is applied. The fabrication of an electrostatic Zach PP is a complex process, which requires several microstructuring techniques and processing in a cleanroom facility, as previously described [27].

The aC films used as HFPPs in our experiments were evaporated from a carbon rod (Ladd Research Industries, Williston, VT, USA) with a Bal-Tec MED 020 evaporator (Leica Microsystems, Wetzlar, Germany) and are similar to the films used in the work of Marko et al. [28]. Films with a thickness of 12 nm were deposited on freshly cleaved mica sheets, floated off the mica in a distilled-water bath and placed on 2-mm discs (Daiwa Techno Systems, Tokyo, Japan) having a 5 × 5 array of 100-μm apertures.

TEM experiments were carried out in a JEOL JEM-3200FSC/PP cryo-TEM (JEOL Ltd., Tokyo, Japan) equipped with a field-emission gun and operated at 300 kV. A cooled sample transfer chamber can store up to 3 cryo samples. The microscope is equipped with two heated

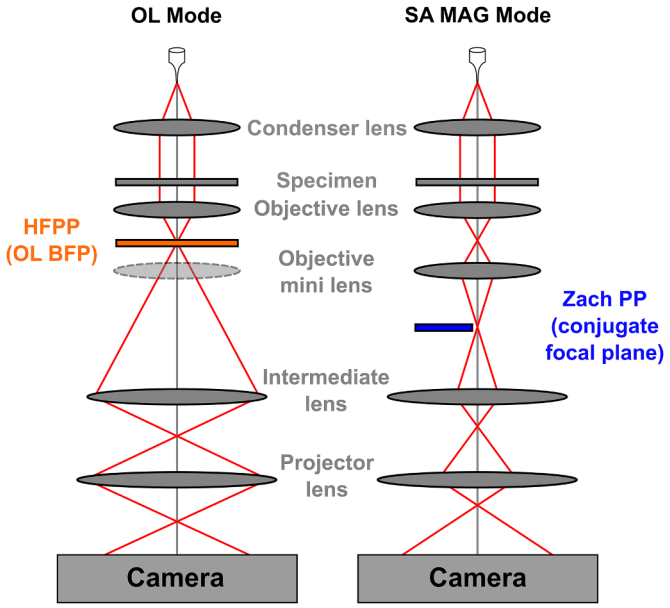

Fig. 1. Electron optical setup of the JEOL JEM-3200FSC/PP cryo-microscope to study phase-contrast formation in TEM using HFPPs and electrostatic Zach PPs. The HFPP is implemented in the BFP of the objective lens and the Zach PP in the SAD plane. The HFPP is operated in normal mode (objective-lens (OL) mode). To operate the Zach PP, the SAD plane can be transformed into a conjugate focal plane by a modified objective mini lens that is used as a transfer lens ("SA MAG" mode). The objective lens is not deactivated in "SA MAG" mode.

(up to 500 °C) piezo-driven PP holders, which are positioned in the objective-lens BFP and also in the selected-area diffraction (SAD) plane (cf. Fig. 1). The HFPP is implemented in the objective-lens BFP (focal length 5 mm), while the electrostatic Zach PP is inserted in the SAD plane. The SAD plane can be transformed into a conjugate focal plane (focal length 15.8 mm) by a modified objective mini lens used as a transfer lens [29]. The objective lens continues to operate in this "SA MAG" mode. The spherical aberration coefficient C_s only worsens from 5.2 to 5.29 mm in this mode. The PP holders are equipped with a separately pumped load-lock system, which enables rapid PP exchange. During the experiments, the HFPP was continuously heated to 260 °C and the Zach PP to 80 °C. The Zach PP was heated to prevent contamination and charging of the PP structure [27]. The PP holder in the SAD plane was especially adapted for the application of a Zach PP by removing the temperature sensor and using its cable feed-through for biasing the PP electrode. A 9-volt battery was used as voltage supply, with a potentiometer in combination with a voltmeter and a switch to change the polarity of the bias. An automatic liquid-nitrogen refilling system keeps the specimen stage at ~100 K. The stage has a tilt range of 140° and long-range piezo translation along the tilt axis, which can be used to shift the sample for focusing and PP adjustment in a remote sample area, without irradiation of dose-sensitive objects in the region of interest. This function is also needed for tracking operations during tilt-series collection for cryo-electron tomography. For imaging, the TEM is equipped with a Gatan K2 Summit direct-electron detector (Gatan Inc., Pleasanton, CA, USA).

TEM images were acquired in dose-fractionation mode with 4 s overall exposure and 0.2 s exposure time per frame. The illumination intensity was set to ~9 e^-/px/s resulting in a total electron dose between 8 and 12 $e^-/Å^2$. Tomographic tilt series were recorded close to focus at 2° intervals within a 120° tilt range using a modified version of SerialEM [30]. Zero-loss energy filtering with a slit width of 20 eV was applied in dose-fractionation mode. The dose per image was less than 1 e^-/px/s for tomographic tilt-series collection, leading to a total dose of ~80 $e^-/Å^2$ for the whole tilt series. All dose-fractionated images were aligned and summed using the Gatan Digital Micrograph Software (Gatan Inc., Pleasanton, CA, USA). For the tomographic tilt series, this was realized using the SerialEM plugin "Align in DM".

Images and tomographic tilt series were recorded from plunge-frozen T4 samples that were mixed with a suspension of 10-nm colloidal Au particles, to serve as alignment markers, and placed on Quantifoil R2/2 and R2/4 grids (Quantifoil Microtools, Jena, Germany) [31].

The application of a PP requires accurate PP alignment and setting of illumination conditions. The HFPP needs to be set up in on-plane condition such that the crossover of the BFP coincides with the PP plane. Since the HFPP cannot be moved in z-direction, the on-plane condition is adjusted using the condenser-lens system. In the standard TEM imaging mode, a small feature (e.g. a particle) on the PP film is imaged in off-plane condition. Similar to STEM probe focusing, the condenser-lens focus is changed until the particle is "infinitely large". During this procedure, any change of particle shape is corrected by the condenser-lens stigmator. By this alignment, the phase-shifting patch should build up as small and round as possible, yielding optimal imaging conditions. The phase-shifting patch forms within 15–30 s at a beam current of ~1 nA, which is a typical value for low-dose cryo-TEM. These conditions provide stable phase-contrast imaging conditions for a few hours of use [28].

For phase-contrast imaging with the electrostatic Zach PP, the on-plane condition is set up in the conjugate focal plane of the microscope by setting the objective mini lens to the "SA MAG" mode. The tip of the Zach-PP rod is then focused to be as sharp as possible using the "diffraction focus", and the condenser lens is adjusted to minimize the ZOB size. Finally, the PP tip is placed at the correct distance from the ZOB using the piezo positioners.

2.2. Image simulation and image processing

For analysis of the image parameters of the experimental PP-TEM images, a MATLAB program (The Mathworks, Natick, MA, USA) written by Hettler et al. [32] was used. The program simulates a database of power spectra with different defocus, astigmatism and phase-shift values. The simulated power spectra are compared with the experimental power spectrum of the acquired PP-TEM image in an adapted pattern-recognition process [33]. The program returns the best-fitting defocus, astigmatism and phase-shift values for the recorded TEM image.

Intensity line profiles were extracted from experimental images for comparison with simulated data. The line profiles were typically averaged over a width of 40 nm (Zach-PP-TEM images) and 25 nm (HFPP-TEM images) for noise reduction.

We used the IMOD [34] software to reconstruct tomograms. Three-dimensional segmentation was performed with the plugin "Trainable Weka Segmentation" of Fiji [35]. The Avizo software (Thermo Fisher Scientific, Waltham, MA, USA) was used for visualization of the segmentation and generation of the videos in the supplementary materials.

Zach-PP and HFPP images were simulated to achieve a thorough understanding of the experimental observations. For this purpose, the object-wave function after transmission through a T4 sample has to be modelled. T4s are described as pure phase objects. The phase of the estimated object-wave function of two perpendicularly oriented T4s embedded in 150-nm-thick vitrified ice, imaged at an electron energy of 300 keV, is shown in Fig. 2a. The complex structure of the T4 head was approximated by a cylinder with a diameter of 85 nm, and the 4-nm periodicity of the helical protein structure of the tail was simplified by equidistantly positioned cuboids with a thickness of 21 nm. For the purpose of simulations, the mean inner potential of the T4 head and tail was assumed to be $V_0 \approx 6$ V, which is comparable to other DNA-based biomolecular complexes, such as nucleosome core particles [36]. The phase shift of the T4 was calculated according to Eq. (1), which results in 0.0125 π/nm, corresponding to a maximum phase shift of ~1.06 π in the center of the head and a maximum phase shift of ~0.26 π in the cuboids of the tail. The T4s are assumed to be embedded in 150 nm of

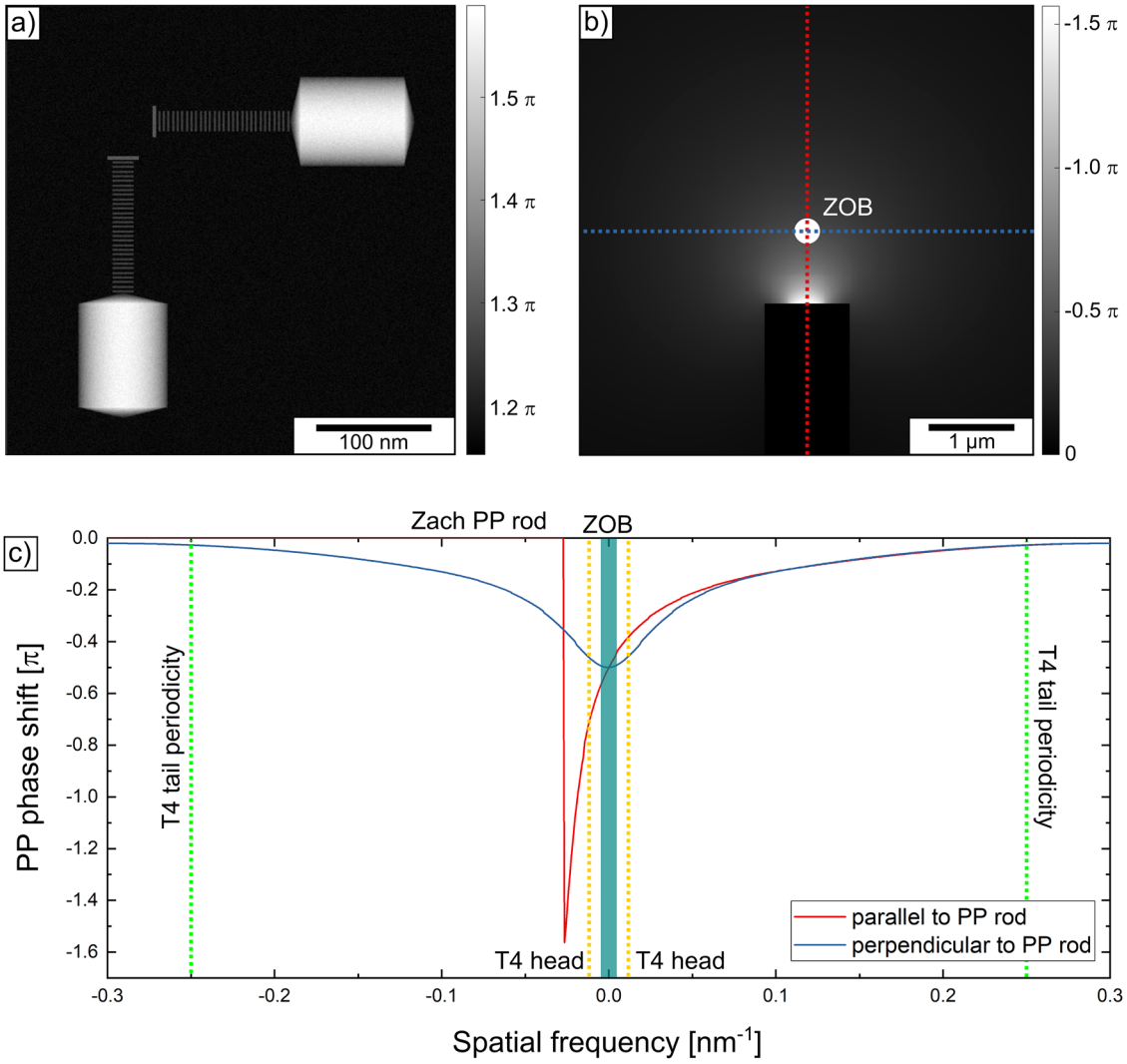

Fig. 2. Model object-wave function of two perpendicularly oriented T4s and phase-shift distribution of the Zach PP. a) Phase of the model object-wave function of two perpendicularly oriented T4s embedded in 150-nm-thick vitrified ice at 300 kV prior to being subjected to a phase-shifting PP. b) Inhomogeneous phase-shift distribution of the Zach PP with a phase shift of $-0.5\ \pi$ imposed on the ZOB electrons at the position marked by the white dot. c) Phase-shift profiles of the Zach PP parallel (red line) and perpendicular (blue line) to the PP rod through the ZOB. The ZOB (blue-green bar), the spatial frequencies of the T4 head (yellow-dotted line) and T4 tail periodicity (green-dotted line) are marked in the diagram.

vitrified ice, which has a mean inner potential of $V_0 \approx 3.5$ V [37]. In the region of the T4, the thickness of the vitrified ice is reduced by the local T4 thickness to achieve a uniform sample thickness of 150 nm. This results in a phase shift of ~1.06 π (black in Fig. 2a) for the pure vitrified ice and a total phase shift of ~1.54 π (white) in the center of the T4 head. We note that T4 heads are not strictly WPOs because the phase of the object-wave function is substantially larger for the T4 head than that of the surrounding ice. Additionally, a random signal with a maximum phase shift of 0.04 π and a maximum amplitude of 0.02 was added to the phase and amplitude of the object-wave function to represent experimental noise. The wave function is available as MATLAB file in the supplementary materials.

Fig. 2b shows the grey-scale-coded inhomogeneous phase-shift distribution of the Zach PP. The phase-shift distribution is based on the calculation of the electrostatic potential by finite-element methods [27] taking into account the electrode dimensions given in Section 2.1. Large phase shifts are represented by the bright region close to the PP tip. The center of the ZOB (marked by a white dot in Fig. 2b) is located at a distance of 850 nm from the end of the Zach-PP rod. The electrostatic potential of the Zach PP is set to achieve a phase shift of $-0.5\ \pi$ at the center of the ZOB, according to the experimental conditions of one of the images shown in Fig. 6. Fig. 2c shows phase-shift profiles through the position of the ZOB, parallel (red curve) and perpendicular (blue curve) to the Zach-PP rod, which differ substantially. A blue-green bar illustrates the ZOB diameter, which is characterized by a full-width half-maximum (FWHM) diameter of 300 nm (0.0048 nm^{-1}) in the conjugate diffraction plane where the Zach PP is located. Distances d in the BFP are converted to spatial frequencies q by the equation

$$q = \frac{d}{\lambda f} \tag{2}$$

with the focal length f equaling 15.8 mm in "SA MAG" mode and 5 mm in normal OL mode. The spatial frequencies of the relevant image features such as the T4 head (0.012 nm^{-1}) and the periodicity in the T4 tail (0.25 nm^{-1}) are marked with yellow- and green-dotted lines. We note that assigning a spatial frequency to an extended object like the T4 head is not strictly correct, however it seems to be a reasonable assumption in the discussion of phase contrast of the T4 heads. The phase-shift profile perpendicular to the Zach-PP rod has a symmetric shape that resembles a Gaussian function with $-0.5\ \pi$ phase shift at the ZOB position. The FWHM of the Gaussian profile at this position is 2.86 µm, which corresponds to a spatial frequency of 0.046 nm^{-1}. The FWHM of

the phase-shift profile decreases with decreasing distance from the tip of the Zach-PP rod. However, the chosen distances of 600–1000 nm between the ZOB and the rod tip were found to be a good compromise between the desired relative phase shift of about $-0.5\ \pi$, the limited positioning accuracy of the PP holder, the prevention of image distortion by charge build-up on the Zach-PP rod and blocking of electrons of the ZOB by the Zach-PP structure. The phase-shift profile parallel to the Zach-PP rod (red line in Fig. 2c) is asymmetric. The negative phase shift decreases with increasing distance from the Zach-PP rod from its maximum value of $-1.56\ \pi$ at the rod tip following a power law with an exponent of ~ -1.4. The Zach-PP rod is not electron transparent and thus blocks electrons covered by the PP rod with spatial frequencies larger than 0.027 nm^{-1} (assuming a 850-nm distance to the ZOB). This leads to single-sideband contrast for spatial frequencies covered by the PP rod.

The phase-shifting patch of the HFPP was assumed to have a Lorentzian shape with a FWHM of 0.015 nm^{-1}, which is slightly larger than the assumed ZOB diameter of 100 nm [8] due to the expected wider spread charge distribution [10] and accounts for the long-range charge distribution. The profile is scaled to account for the experimentally determined phase shift of $-0.7\ \pi$ at its maximum. We note that the Gaussian phase-shift profile of the Zach PP perpendicular to the Zach-PP rod (blue line in Fig. 2c) is considerably wider at the position of the ZOB.

For TEM image simulations, the Fourier transform of the object-wave function was multiplied by the contrast transfer function, the spatial envelope and the aperture function. The contrast transfer function is given by $\exp(\chi)$ with the overall phase shift

$$\chi = \pi \Delta f \lambda q^2 + \frac{\pi}{2} C_s \lambda^3 q^4 + \varphi_{PP}(q) \tag{3}$$

where Δf is defocus, and the spherical aberration coefficient C_S is 5.2 mm for the JEM-3200FSC/PP in normal OL mode or 5.29 mm in "SA MAG" mode. A Lorentzian phase-shift distribution $\varphi_{PP}(q)$ is assumed for the HFPP with a FWHM of 0.015 nm^{-1}. For the Zach PP, the spatial-frequency dependence of $\varphi_{PP}(q)$ according to Figs. 2b,c is taken into account with phase shifts adjusted to the measured values for the ZOB. The strong gradient of the phase shift across the ZOB (red line in Fig. 2c) was modelled by simulating images for different distances between the ZOB and the PP tip. These images were incoherently summed using Gaussian weighting factors. Simulated TEM images were obtained by consecutive inverse Fourier transformation and calculation of the square value of the image-wave function. The weighted-focal-series method was used [38] to take partial temporal coherence into account. The simulations were performed using custom MATLAB software that is available in the supplementary materials together with an information file, the object-wave function that was used and the Zach-PP phase-shift distribution.

3. Results and discussion

Section 3 is subdivided into two parts. In Section 3.1, we present the analysis of HFPP and Zach-PP phase-contrast in TEM images. SubSection 3.1.1 contains a direct comparison of experimental conventional TEM images with HFPP and Zach-PP images, while subSections 3.1.2 and 3.1.3 present a quantitative analysis of HFPP and Zach-PP images by comparison of experimental and simulated images. Section 3.2 is devoted to the results of HFPP and Zach-PP tomography.

3.1. Analysis of phase contrast in HFPP- and Zach-PP-TEM images

3.1.1. Comparison of experimental conventional TEM and phase-contrast TEM images

Fig. 3 compares images of an ice-embedded T4 sample acquired close to focus by conventional (C) TEM, HFPP TEM and Zach-PP TEM. The weak T4 contrast in the CTEM image (Fig. 3a) does not show any structural details, and only strongly scattering Au nanoparticles are visible. Fig. 3b presents a HFPP-TEM image of the same sample region acquired with a phase shift of $-0.7\ \pi$. The T4s show strong contrast, and the structure of their tails with the baseplate, the long tail fibers and the collar can be easily recognized. Most T4s are filled with DNA, with their heads showing uniform dark contrast (representative example marked with a black arrow in Fig. 3b). The capsid of the head does not differ in contrast from the packaged DNA inside the T4 head. Apart from that, three T4s have an empty head with brighter contrast (representative example marked with a white arrow) indicating that they have already gone through the infection cycle and have lost the DNA in the head. For the empty T4 heads, the protein shell of the capsid is clearly visible and appears as a line with dark contrast outlining the head. We also note that a bright halo is visible around the T4 heads. The significantly improved contrast in the HFPP image compared to the CTEM image is also evidenced by the clearly improved contrast transfer for low spatial frequencies in the power spectrum inserted in Fig. 3b.

Figs. 3c-f show a voltage series of Zach-PP-TEM images of the same T4 sample. The distance between the Zach-PP rod and the ZOB was ~600 nm, corresponding to a spatial frequency of 0.019 nm^{-1} according to Eq. (2). In the center of the imaged sample region, three T4s (marked with a white arrow in Fig. 3e) are present, with contracted tail sheaths and the DNA in their heads partially ejected. In the lower left corner, a complete T4 with a filled head is present (marked with a black arrow in Fig. 3e) and two more fragmented T4s are observable on the left-hand side. Fig. 3c shows a Zach-PP-TEM image without applied voltage. The T4 contrast is nevertheless improved compared to the T4 in the CTEM image (cf. Fig. 3a), and a small negative phase shift of $-0.24\ \pi$ is measured due to electrostatic charging of the insulating shielding material in the Zach-PP rod. The Zach-PP rod is clearly observable in the inserted power spectrum, and enhanced image contrast results from a slightly inhomogeneous contrast transfer for mid-range spatial frequencies. Furthermore, the Zach-PP rod obstructs electrons in the BFP inducing single-sideband contrast for small image features. Fig. 3d shows a Zach-PP-TEM image of the same sample region with 1 V applied, leading to a total phase shift of $0\ \pi$. In this image, the T4s show minimum contrast, and the tails and long tail fibers are almost indistinguishable from the background. The low contrast transfer is also observable in the corresponding power spectrum. Some remaining contrast can be attributed to the presence of the PP rod and a remnant electrostatic potential close to the PP rod. The application of -1 V (Fig. 3e) generates a phase shift of $-0.5\ \pi$, yielding optimum contrast in the Zach-PP voltage series. The image contrast is comparable to the contrast in the HFPP image in Fig. 3b (cf. the T4 marked by a white arrow). Note that the contrast of the capsids of the partially emptied T4 heads, the tails and the long tail fibers is significantly improved. A close inspection of the centers of the partially emptied T4 heads reveals residual DNA strings inside the capsids. In comparison to the uniform contrast of the filled T4 heads in the HFPP image in Fig. 3b, the filled T4 heads in Fig. 3e show a slight intensity variation, which depends on the orientation of the T4 with respect to the Zach-PP rod. The application of 2 V generates a positive phase shift of $0.25\ \pi$ (Fig. 3f). This results in contrast inversion compared to Fig. 3e, leading to bright contrast of the T4 tails, the tail fibers and the capsids of the emptied heads. The contrast of the filled T4 head and Au nanoparticles is inverted similarly. The power spectra of the images in Fig. 3e,f show strong contrast transfer apart from the region covered by the PP rod. Furthermore, all Zach-PP images (Figs. 3c-f) show a weakly oscillating intensity in the amorphous-ice regions, arising from the imaged objects along the direction of the Zach-PP rod (the orientation of the Zach-PP rod is indicated in the inset of Fig. 3c). The intensity oscillations are almost invisible in Fig. 3e, which was taken under optimum phase-shift conditions.

3.1.2. Analysis of HFPP-TEM images in experiment and by simulations

To further investigate contrast enhancement and artifacts associated

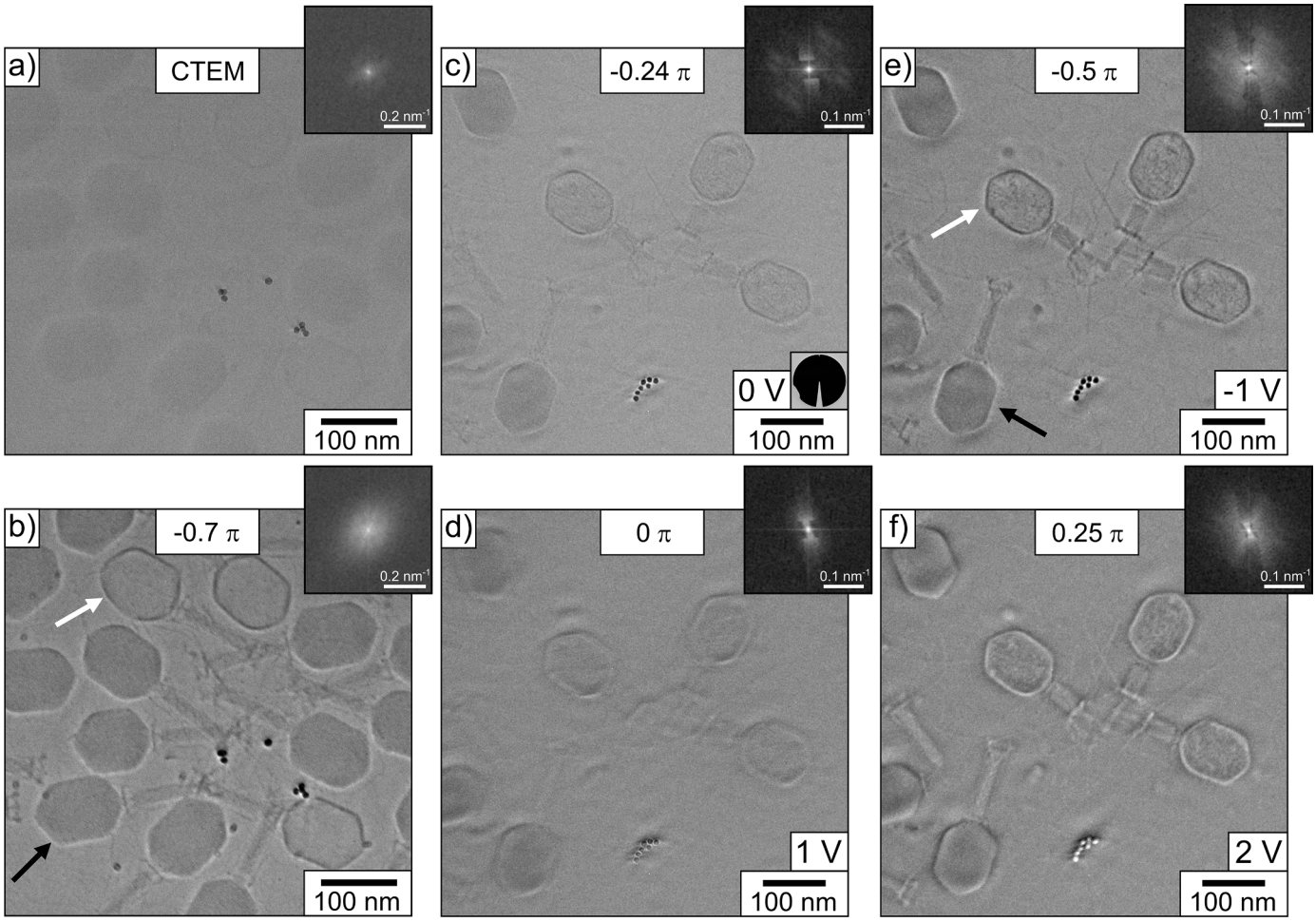

Fig. 3. 300 keV low-dose CTEM and PP-TEM images of an ice-embedded T4 sample acquired with a HFPP or a Zach PP close to focus including corresponding power spectra. a) CTEM image without PP recorded with an electron dose of ~16 $e^-/Å^2$ and b) HFPP-TEM image taken with a phase shift of $-0.7\ \pi$ and an electron dose of ~12 $e^-/Å^2$. c-f) Zach-PP-TEM voltage series with c) 0 V (phase shift $-0.24\ \pi$), d) 1 V (0 π), e) -1 V ($-0.5\ \pi$) and f) 2 V (0.25 π), acquired with an electron dose of ~8 $e^-/Å^2$. The orientation of the Zach PP in c-f) is indicated in c). A representative T4 with a DNA-filled head is marked with a black arrow and a T4 with a partially emptied head is indicated with a white arrow in b) and e).

with HFPPs, intensity line profiles of the DNA-filled T4 heads and the 4-nm periodicity in the tail were investigated. Fig. 4 shows an enlarged view of a T4 in CTEM (Fig. 4a) and HFPP-TEM images ($-0.7\ \pi$, Fig. 4b), which were both acquired close to focus with an electron dose of ~12 $e^-/Å^2$. Intensity line profiles across the T4 head are compared in Fig. 4c. The black line corresponds to the CTEM image in Fig. 4a (the profile direction is marked with a black arrow). The contrast seems weak because the intensity profile does not show a step at the transition between ice and the T4 head. The strongly enhanced contrast of the T4 head in the HFPP-TEM image in Fig. 4b is characterized by the pronounced intensity difference between the head and the surrounding ice along the purple line profile (the profile direction is marked with a purple arrow in Fig. 4b). The halo around the T4 head in Fig. 4b corresponds to the maxima in the line profile at the head boundaries. The halo results from the smooth gradient of the phase-shift profile that is generated by the charged patch of the HFPP [8,12]. The slight intensity difference of the right and left halo maxima originates from a slight drift of the PP holder during image acquisition [12]. Different background intensities of the two line profiles result from electron scattering in the HFPP film, which slightly reduces the overall intensity. The fact that the Zach PP has no film is an advantage over the HFPP. While the T4 head with its diameter of 85 nm is a relatively large extended feature (and possibly not strictly a WPO), the 4-nm periodicity in the tail facilitates evaluation of contrast enhancement by a HFPP for small features. A comparison of intensity profiles along the tail is presented in Fig. 4d for the CTEM image (blue line, profile direction marked with a blue arrow in Fig. 4a) and the HFPP-TEM image (red line, profile direction marked with a red arrow in Fig. 4b). While the maxima and minima of the 4-nm periodicity of the tail are difficult to recognize in the noisy line profile of the CTEM image, they clearly appear in the line profile of the HFPP image. Figs. 4e,f show simulation results of an in-focus HFPP image based on the object-wave function shown in Fig. 2a, with a maximum phase shift of $-0.7\ \pi$ according to the experimental HFPP-TEM image in Fig. 4b. The image shows high contrast for the T4 head and the 4-nm periodicity in the tail. The T4 heads are surrounded by a bright halo as observed in the experimental image Fig. 4b. Due to the symmetrical phase-shift profile of the HFPP, the contrast does not depend on the orientation of the bacteriophage. The intensity line profile across one of the T4 heads along the purple arrow in Fig. 4e shows the same features as the experimental data in Fig. 4c, with intensity maxima at the head boundaries leading to the bright halo. Fig. 4 shows that the application of a HFPP yields contrast enhancement for larger and smaller features. The phase-shift profile of the HFPP extends over the complete ZOB diameter and causes a relative phase shift even for comparatively low spatial frequencies. The maximum object size, which can be imaged with phase contrast, is not limited by a sharp cut-on frequency for the HFPP.

3.1.3. *Analysis of Zach-PP-TEM images in experiment and by simulations*

Contrast formation with the Zach PP results from a combination of

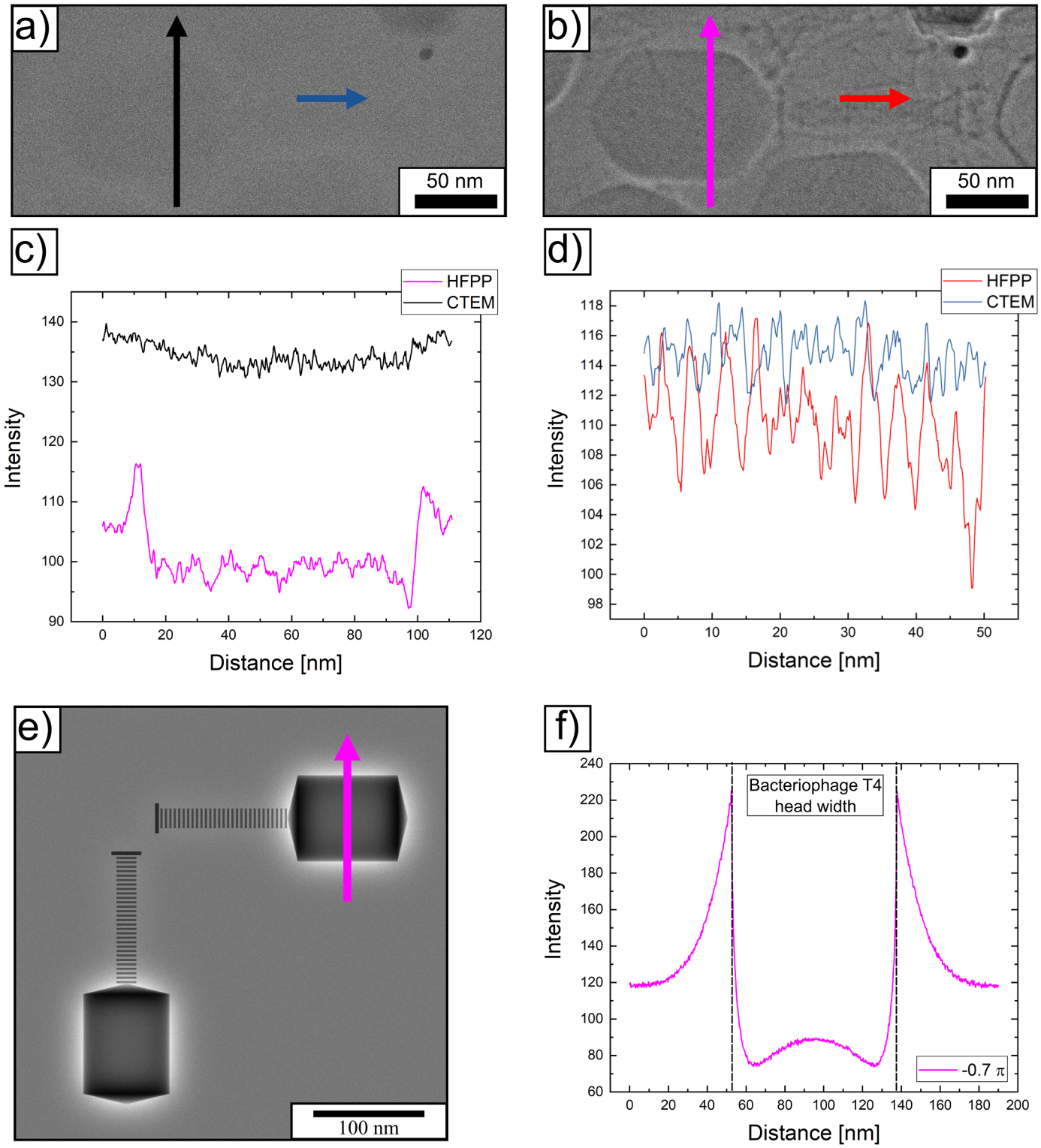

Fig. 4. Contrast enhancement of a T4 head and tail by HFPP TEM. a) Low-dose in-focus CTEM image without a PP and b) low-dose in-focus HFPP image of a T4 with a phase shift of $-0.7\ \pi$. c) A line profile of the T4 head from the CTEM image is marked with a black arrow in a) and one from the HFPP image is marked with a purple arrow in b). d) A line profile of a T4 tail from the CTEM image is marked with a blue arrow in a) and one from the HFPP image is marked with a red arrow in b). e) Simulated in-focus HFPP image with a phase shift of $-0.7\ \pi$. f) Simulated intensity line profile across the T4 head marked with an arrow in e). The head boundaries are marked by dashed lines in f).

the gradual phase-shift profile and blocking of electrons by the Zach-PP rod, which leads to an orientation-dependent contrast of the imaged object. These effects are analyzed in detail in the images in Fig. 5 and Fig. 6. Fig. 5 shows experimental (Figs. 5a,c) and simulated (Figs. 5b,d) in-focus Zach-PP images of a T4 with a DNA-filled head, with the Zach-PP rod oriented parallel to the T4 (cf. inset in Figs. 5a,b). The distance between the Zach-PP rod and the ZOB was ~600 nm, corresponding to a spatial frequency of 0.019 nm^{-1}. A voltage of -1 V at the Zach PP yields a negative phase shift of $-0.5\ \pi$ in the image in Fig. 5a. Fig. 5c was taken with a voltage of 2 V, resulting in a positive phase shift of

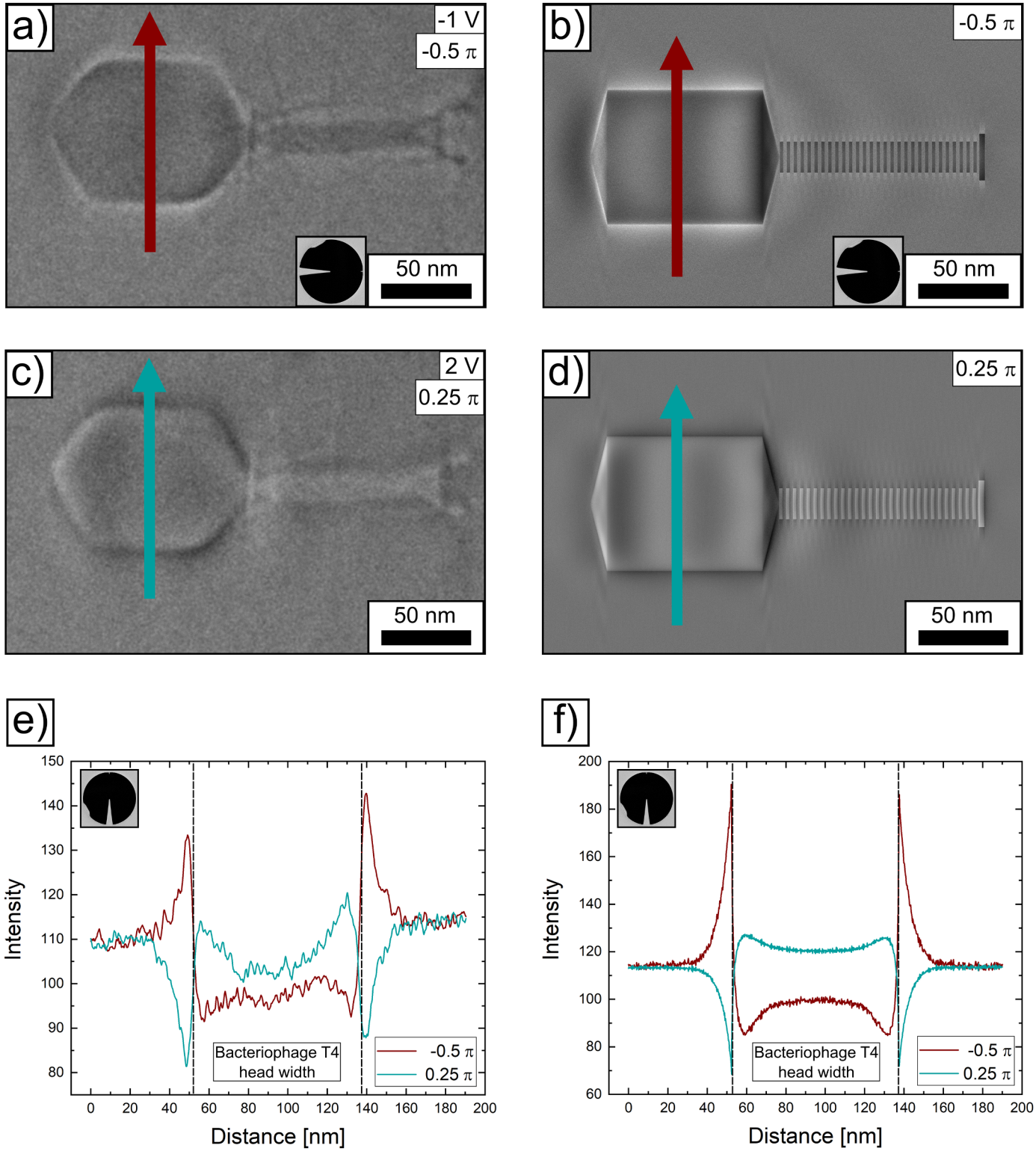

Fig. 5. Contrast enhancement by a Zach PP analyzed by intensity line profiles across a T4 head in experimental and simulated Zach-PP-TEM images for two different applied voltages with the Zach-PP rod oriented parallel to the T4. a) Experimental and b) simulated Zach-PP-TEM image with a negative phase shift of $-0.5\ \pi$ (-1 V). c) Experimental and d) simulated Zach-PP-TEM image with a positive phase shift of $0.25\ \pi$ (2 V). The orientation of the Zach PP is indicated in a) and b). The electron dose was $\sim 8\ e^{-}/Å^{2}$. e,f) Line profiles across the T4 head from e) the experimental Zach PP images in a) and c) are compared with line profiles across the T4 head from f) the simulated Zach PP images in b) and d), with a phase shift of $-0.5\ \pi$ (brown line) and $0.25\ \pi$ (blue line).

$0.25\ \pi$. To achieve a more detailed understanding of phase-contrast formation, corresponding simulated images based on the model object-wave function in Fig. 2a are presented in Figs. 5b,d. A phase-shift distribution of the Zach PP was assumed as shown in Figs. 2b,c with a phase shift of $-0.5\ \pi$ and $0.25\ \pi$ for the ZOB electrons according to the experimental conditions. Experimental and simulated images are in good agreement. Fig. 5e shows intensity line profiles across the T4 head extracted from the experimental images (brown and blue arrows in

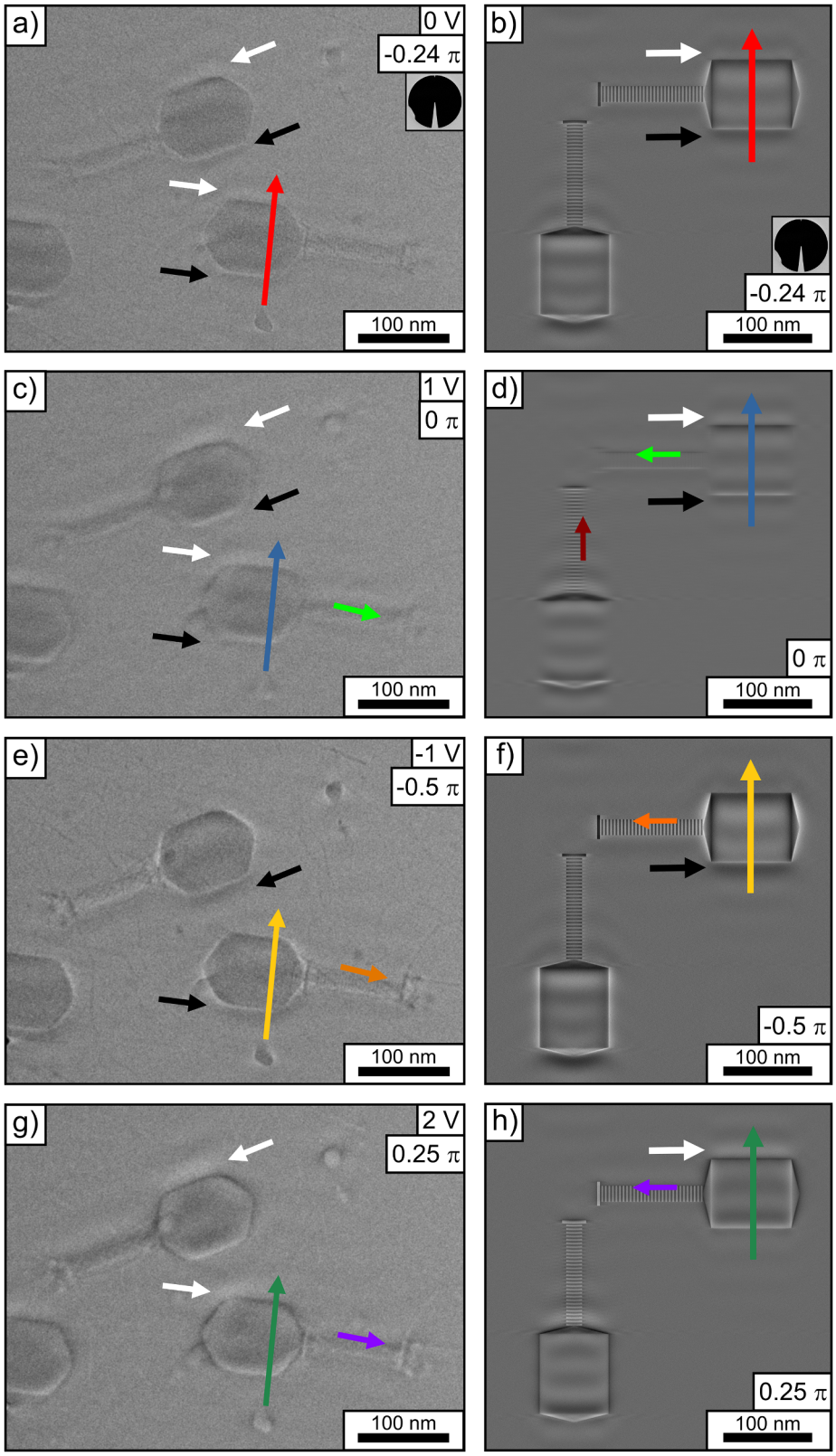

Fig. 6. Low-dose experimental and simulated Zach-PP-TEM images taken for different voltages with the Zach-PP rod oriented perpendicular to the T4 as indicated in a,b). a,b) Experimental and simulated Zach-PP-TEM images for an applied voltage of 0 V ($-0.24\ \pi$), c,d) 1 V ($0\ \pi$), e,f) -1 V ($-0.5\ \pi$) and g,h) 2 V ($0.25\ \pi$). The electron dose was $\sim 8\ e^{-}/Å^{2}$.

Figs. 5a,c). The corresponding profiles from the simulated images are presented in Fig. 5f, where the head boundaries are marked by black lines. The brown intensity profiles (phase shift $-0.5\ \pi$) show two sharp maxima at the outer head boundaries extending into the amorphous ice region, which appear as bright halo in Figs. 5a,b. Accordingly, the intensity of the blue profiles (phase shift $0.25\ \pi$) is inverted and shows

two sharp minima (cf. dark halos in Figs. 5c,d).

The images and intensity profiles obtained with the Zach PP oriented parallel to the T4 in Fig. 5 resemble the HFPP images in Fig. 4. Halos are present at the outer boundaries of the T4 head in the Zach-PP and HFPP images. The halo in the Zach-PP images can be ascribed to the Gaussian phase-shift profile of the Zach PP perpendicular to the Zach-PP rod (cf. Fig. 2c, blue line), similar to the phase-shift profile of a HFPP. In contrast to HFPP images, an intensity inversion of the extrema at the head boundaries can be induced if the sign of the phase shift is inverted. Furthermore, the contrast enhancement in the T4 head in the Zach-PP images resembles on first sight the contrast enhancement in the HFPP image. However, the Gaussian phase-shift profile of the Zach PP is rather broad (cf. Fig. 2c) compared to the HFPP phase-shift profile with a FWHM of 0.015 nm^{-1}. Hence, not only the phase of ZOB electrons is shifted in Zach-PP images but also the phase of scattered electrons in a certain spatial-frequency band around the ZOB. This reduces phase contrast of large structures due to the gradual decrease of the relative phase shift between unscattered and scattered electrons. A specific cut-on frequency that determines the maximum object size for phase-contrast imaging cannot be precisely defined but only a soft cut-on frequency range. Considering simulated phase-shift profiles as in Fig. 2c, the soft cut-on frequency range can be defined by a spatial-frequency band of relative phase shifts between 0.2 π and 0.4 π with respect to the ZOB electrons [27]. With a distance of 600 nm between the PP rod and the ZOB and a phase shift of −0.5 π for the ZOB electrons, the soft cut-on frequency range perpendicular to the PP rod covers spatial frequencies between 0.104 and 0.026 nm^{-1}. This means that phase-contrast imaging is possible for periodic (or particulate) objects with a maximum repeat or particle size of 38.5 nm. Phase contrast is enhanced with smaller periodicities. Thus, the T4 head seems too large to be imaged with phase contrast, and the head contrast may be caused by effects of the phase-shift profile parallel to the Zach-PP rod, as discussed in detail in the context of Figs. 6 and 7. In fact, the effect of the Zach PP can be recognized in Figs. 5a-d by the intensity oscillation in the head perpendicular to the brown and blue arrows. Finally, we note that artifacts induced by the Zach-PP rod itself on the T4 contrast are negligible in this orientation because spatial frequencies are not blocked and single-sideband contrast does not occur.

The 4-nm periodicity in the T4 tails is clearly visible in the simulations (Figs. 5b,d) and appears with dark contrast for a negative (−0.5 π) phase shift and bright contrast for a positive (0.25 π) phase shift. Strong phase contrast is expected for the spatial frequency of the tail, as indicated by the green-dotted lines in Fig. 2c. However, the 4-nm periodicity is absent in the experimental images, which can be explained by a slightly tilted orientation of the tail with respect to the incident electron beam.

In the following, we focus on phase contrast and artifacts caused by the presence of the Zach-PP rod. For this purpose, we present in Fig. 6 in-focus experimental and simulated images of a Zach-PP voltage series. The Zach-PP rod is oriented perpendicular to the T4 in all images of Fig. 6 (cf. inset in Figs. 6a,b). In the simulations, only the T4 in the right part of the image is considered (Figs. 6b,d,f,h). Fig. 6a represents imaging without an applied voltage. As in Fig. 3c, a small negative phase shift of −0.24 π was measured resulting from unavoidable charging of the insulating material in the Zach-PP rod. We observe intensity variations with dark contrast (black arrows) and bright contrast (white arrows) slightly outside of the T4 heads in Fig. 6a, which are well reproduced in the simulated image in Fig. 6b. Fig. 6c was acquired with 1 V applied to the Zach PP, resulting in a phase shift of 0 π. The positive voltage compensates negative charging of the insulating material in the Zach PP. With a resulting phase shift of 0 π, the image in Fig. 6c is particularly interesting with respect to possible artifacts that are introduced by the Zach-PP rod itself. Again, the simulated image in Fig. 6d agrees well with the experimental one.

Contrast details are more clearly visualized in intensity line profiles across the T4 heads (cf. red arrows in Figs. 6a,b and blue arrows in Figs. 6c,d). Fig. 7a contains experimental intensity line profiles from the experimental images in Figs. 6a,c for a phase shift of −0.24 π (red line) and 0 π (blue line). Simulated profiles in Fig. 7b from the simulated images in Figs. 6b,d agree well with the experimental profiles. Prominent intensity extrema in the line profiles are indicated with numbered grey-dotted lines. The intensity features in the blue profiles (0 π phase shift) in Figs. 7a,b reveal artifacts due to the presence of the Zach-PP rod. Mark 2 in Figs. 7a,b corresponds to the dark contrast near the lower boundary of the T4 head (black arrows in Figs. 6a-d), which is followed by a sharp maximum (mark 3). The contrast is inverted at the opposite side of the head, where a sharp minimum (mark 6) near the upper head boundary is followed by a broad intensity maximum (mark 7) (white arrows in Figs. 6a-d). We note that contrast inversion of the extrema at opposite head boundaries does not occur in the images in Figs. 5a,c with the Zach PP oriented parallel to the T4. Contrast inversion is assigned to single-sideband contrast because the spatial-frequency spectrum of the head boundaries is intercepted by the Zach PP. Within the heads, intensity oscillations with a periodicity of ~38 nm (marks 4 and 5 in Figs. 7a,b) are observed, which also extend into the adjacent ice, with decreasing intensity (marks 1 and 8) in the direction of the PP rod. This periodicity correlates with the distance between the PP rod and the ZOB in the BFP (~850 nm/~0.027 nm^{-1}, corresponding to a ~37 nm periodicity). The slight shift of the oscillations in the red and blue profiles is induced by the phase-shift difference of 0.24 π between the two images. The simulations also reveal that the sharp extrema are located exactly at the head boundaries (black dashed lines in Figs. 7a,b).

Experimental and simulated images for a phase shift of −0.5 π (−1 V at Zach PP) are shown in Figs. 6e,f and for a phase shift of 0.25 π (2 V at Zach PP) in Figs. 6g,h. Intensity line profiles across the T4 head from the experimental images (yellow and green arrows in Figs. 6e,g) are shown in Fig. 7c for a phase shift of −0.5 π (yellow line) and for a phase shift of 0.25 π (green line). Simulated line profiles in Fig. 7d from the images in Figs. 6f,h reproduce the experimental data well. The features in these profiles generally agree with the features of the profiles in Figs. 7a,b. Sharp intensity extrema at opposite head boundaries (marks 3 and 6) occur. The oscillating intensity with 38-nm periodicity within the head and in the surrounding ice is also present, although with low intensity, in Fig. 6e, which was taken under optimum conditions (−0.5 π). The extrema of the 38-nm periodicity shift in opposite directions due to the sign change of the phase shift. This roughly results in the inversion of the yellow and green profiles due to the large phase-shift difference of 0.75 π. The large phase-shift difference, in combination with the sharp contrast features at the head boundaries, affects the extrema intensities. For example, the intensity minimum at mark 2 in the green profiles almost disappears, whereas the maximum at mark 7 is intensified (cf. the white arrows in Figs. 6g,h). The opposite effect is observed for the yellow profiles with a pronounced minimum at mark 2 and a low maximum at mark 7 (cf. black arrows in Figs. 6e,f).

We note that numerical methods for the reconstruction of amplitude information partially blocked by the electrode-supportive PP structure developed for Boersch-PP-TEM images exist [39,40] and are applicable to Zach-PP-TEM images of WPOs as well. The technique could reduce artifacts introduced by the Zach-PP rod and restore the single-sideband to full-sideband contrast.

The intensity within the T4 heads is mainly determined by the 38-nm periodicity because objects with a size of 85 nm (0.012 nm^{-1}) cannot be expected to experience a significant phase shift. According to Fig. 2c, only a small phase change for structural features with this spatial frequency (yellow-dotted lines) occurs with respect to the ZOB electrons. Nevertheless, the spatial-frequency range that can be imaged with phase contrast was extended by a factor of ~3 towards lower spatial frequencies in this work because the Zach PP was positioned in the magnified diffraction plane. For a distance of 850 nm between PP rod and ZOB and a phase shift of −0.5 π for the ZOB electrons, the soft cut-on frequency range of the phase-shift profile parallel to the PP rod

covers spatial frequencies between 0.129 and 0.025 nm^{-1}, corresponding to object sizes from 7.8 to 40 nm.

The 4-nm tail periodicity is not adversely affected by the given cut-on frequency range. We will discuss tail contrast by considering the intensity line profiles in Figs. 7e-j. The tail periodicity is hardly recognizable in the experimental profile in Fig. 7e, as expected for 0 π

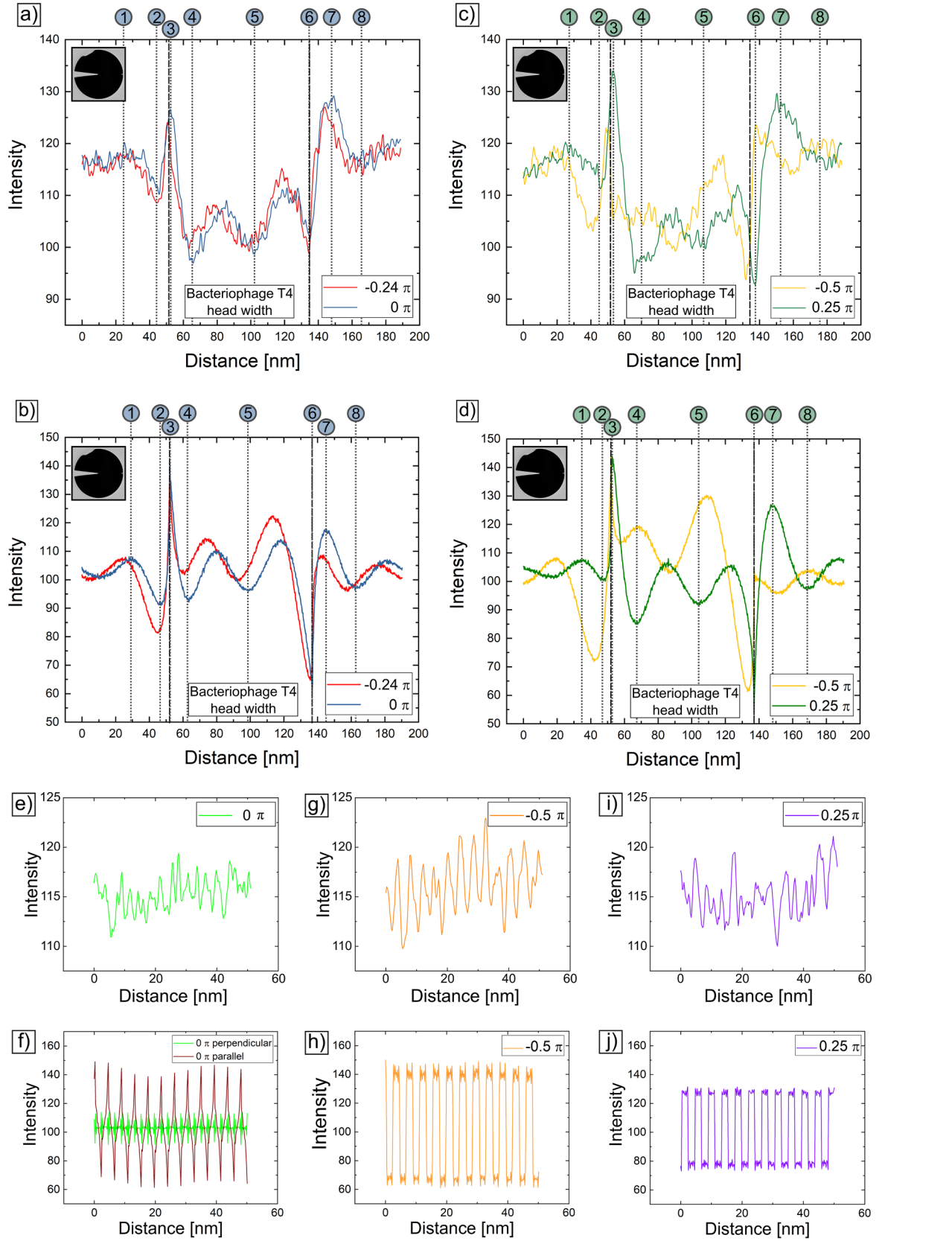

(caption on next page)

Fig. 7. Contrast enhancement by Zach-PP TEM of a T4 head and tail visualized by intensity line profiles from experimental and simulated images in Fig. 6, with the Zach-PP rod oriented perpendicular to the T4. a) Line profiles across the T4 head from the experimental Zach-PP images (cf. the red and blue arrows in Figs. 6a,c) and b) line profiles from the simulated Zach-PP images (cf. the red and blue arrows in Figs. 6b,d) with a phase shift of $-0.24\ \pi$ (red lines) and $0\ \pi$ (blue lines). c) Line profiles across the T4 head from the experimental Zach-PP images (cf. the yellow and green arrows in Figs. 6e,g) and d) line profiles from the simulated Zach-PP images (cf. the yellow and green arrows in Figs. 6f,h) with a phase shift of $-0.5\ \pi$ (yellow lines) and $0.25\ \pi$ (green lines). The orientation of the Zach PP is indicated in a-d). e,f) Intensity line profiles of a T4 tail with a phase shift of $0\ \pi$ from the experimental and simulated images in Figs. 6c,d (green arrows). g,h) Intensity line profiles of a T4 tail with a phase shift of $-0.5\ \pi$ from the experimental and simulated images in Figs. 6e,f (orange arrows) and i,j) intensity line profiles of a T4 tail with a phase shift of $0.25\ \pi$ from the experimental and simulated images in Figs. 6g,h (purple arrows). The brown line profile in f) corresponds to the brown arrow in Fig. 6d with the Zach-PP rod oriented parallel to the T4 tail.

(green arrow in Fig. 6c). Fig. 7f contains line profiles from the simulated image in Fig. 6d with the T4 tail oriented perpendicular (green arrow) and parallel (brown arrow) to the PP rod. The brown line in Fig. 7f shows pronounced tail contrast even without phase shift due to single-sideband contrast because the tail´s spatial frequency is blocked by the PP rod. Phase contrast of the tail is absent for the green profile, in agreement with the experimental data. The experimental and simulated profiles in Figs. 7g,h, taken from Figs. 6e,f (orange arrows), show pronounced tail contrast, as expected for a phase shift of $-0.5\ \pi$. Also anticipated is weaker tail contrast for a $0.25\ \pi$ phase shift (cf. Figs. 7i,j). The experimental profiles show in general lower contrast compared to simulations due to the low signal-to-noise ratio and possible misalignment of the incident electron-beam with respect to 4-nm tail features. The contrast of small-scale periodicities also benefits from single-sideband contrast if the features are oriented parallel to the Zach-PP rod. We note that the simulated intensity line profile of the tail for single-sideband contrast (brown curve in Fig. 7f) shows sharp maxima, as opposed to true phase contrast in Fig. 7h, where a rectangular pattern is observed. The observations demonstrate pronounced contrast enhancement of small features such as the 4-nm tail periodicity, if the phase shift of the Zach PP is adjusted to the optimum value.

3.2. Electron tomography

The benefits of contrast enhancement by PPs in electron tomographic reconstructions of T4s are demonstrated in Fig. 8. Tomographic tilt series were acquired close to focus with a HFPP (phase shift $-0.7\ \pi$) and a Zach PP (phase shift $-0.5\ \pi$). Both 120°-tomographic tilt series were recorded with zero-loss energy filtering (slit width 20 eV) and a total electron dose of ~80 $e^-/Å^2$. An anisotropic diffusion filter [41] was used to reduce noise without removing significant image details. The tomograms (cf. Video A.1 for the HFPP and Video A.2 for the Zach PP) and three-dimensional segmentations (cf. Video A.3 for the HFPP and Video A.4 for the Zach PP) are available in the supplementary materials.

Summations of three slices with 2-nm thickness of a tomographic reconstruction of a T4 sample are presented in Fig. 8a (HFPP) and Fig. 8b (Zach PP). Both tomographic slices show a T4 with strong contrast and good visibility of the 4-nm periodicity in the tail. The HFPP tomogram contains a small part of an emptied T4 head (white arrow in Fig. 8a), with strong contrast of the T4 capsid. The DNA-filled T4 heads (an example is marked by the black arrow in Fig. 8a) exhibit uniform dark contrast in their center and are surrounded by the typical halo due to the phase-shift profile of the HFPP. The emptied T4 head (white arrow in Fig. 8b) in the Zach-PP image shows strong capsid contrast as well. The weak oscillating intensity within the head and in the amorphous ice region around the head as previously discussed for single Zach-PP images (cf. Figs. 3 and 6) is not observable because the tomographic reconstruction algorithm suppresses it. Minima and maxima at the head boundaries are intensified.

Overall, the tomographic tilt series recorded with the Zach PP yields results that are of similar quality as in the HFPP tomogram. An important benefit of the Zach PP in tomographic tilt-series collection is the adjustable phase shift. Phase contrast depends on the phase shift that

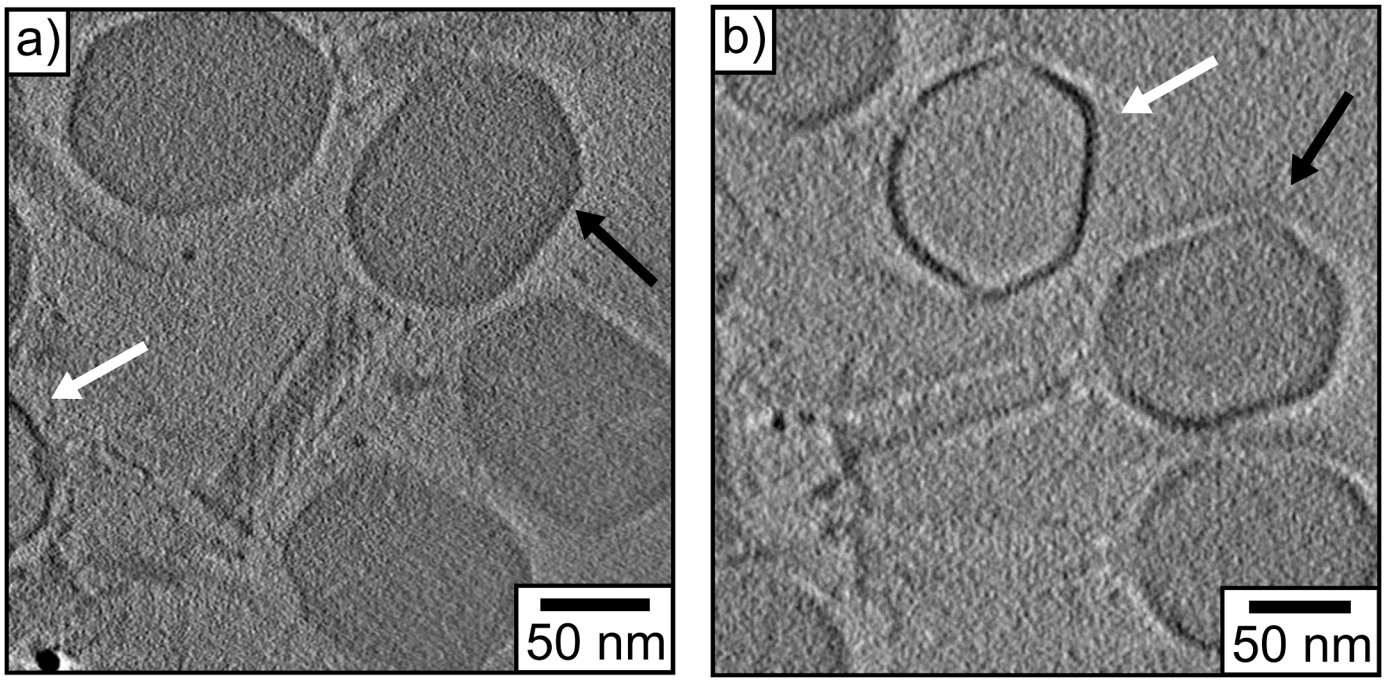

Fig. 8. Slices of electron tomograms of T4 acquired with HFPP and Zach PP close to focus and with zero-loss energy filtering (total electron dose ~80 $e^-/Å^2$). Summations of three 2-nm-thick slices of an electron-tomographic reconstruction acquired with a tomographic tilt series using a) HFPP-TEM imaging and b) Zach-PP-TEM imaging.

the objects in the sample impose on the traversing electron wave. With increasing tilt angle, the distribution of the phase shift by the sample changes due to its changed geometry and the increasing path length of the electrons traversing the sample. Thus, the adaption of the phase shift induced by the PP is beneficial. During the acquisition of the tilt series, the phase shift induced by the Zach PP was readjusted by inspection of the Thon rings in the power spectrum of a live-view defocused image (stage-shifted "Trial" mode in SerialEM). Readjustment of the phase shift is not possible for the HFPP, which in any case results in a change of phase contrast during the acquisition of the tilt series and leads to deviations from optimum conditions for phase-contrast imaging, especially during tilting.

4. Summary

We analyzed the performance of hole-free phase plates (HFPPs) and Zach PPs for phase-contrast cryo-transmission electron microscopy (TEM) of ice-embedded T4 bacteriophages (T4s) by experimental and simulated in-focus images. We obtained good agreement between simulated and experimental PP-TEM images by taking into account realistic phase-shift distributions induced by the applied PPs and a spatially extended Gaussian zero-order beam in the plane of the PP. A symmetric Lorentzian phase-shift profile was assumed for the HFPP with a width corresponding to the zero-order beam diameter of 100 nm in the back focal plane. High and low spatial frequencies, corresponding respectively to the T4 tail and head, can be well-imaged with phase contrast. The symmetric phase-shift profile of the HFPP does not induce any orientation-dependent artifacts. However, a bright halo surrounding the imaged objects is observed due to the gradual phase-shift profile. The HFPP phase shift is determined by the experimental conditions and can only be influenced indirectly by changing the HFPP temperature.

In contrast, the electrostatic Zach PP allows tuning of the phase shift by the applied voltage, which can be beneficial for certain applications. Furthermore, the design of the Zach PP does not lead to damping of the intensity of the traversing electrons, in comparison to the electron scattering in the thin HFPP film. However, the asymmetric phase-shift profile of the Zach PP in combination with electron obstruction by the Zach-PP rod induces artifacts, which depend on the object orientation with respect to the Zach-PP rod. Like the HFPP, the Zach PP is characterized by a soft cut-on frequency range, which minimizes fringing artifacts. By implementing the Zach PP into the magnified focal plane of an adapted transmission electron microscope, phase contrast can be achieved for objects up to a size of 40 nm. In our experience, troublesome unwanted charging of the PP rod was avoidable.

An electrostatic Zach PP was used for cryo-electron tomography for the first time and compared to the results from tomography with a HFPP. The quality of reconstructed tomograms from both PPs is similar because orientation-dependent artifacts from the Zach PP are suppressed by the reconstruction procedure. In addition, the adjustable phase shift of the Zach PP is advantageous because the phase shift can be kept constant in each image, despite the change of the projected sample thickness.

Declaration of Competing interest

The authors declare that they have no known competing financial interests or personal relationships that could have appeared to influence the work reported in this paper.

Acknowledgments

The authors acknowledge Dr. Frank Maley of Wadsworth Center for providing the T4 bacteriophages in suspension and Dr. Matthias Meffert of the LEM for help with the three-dimensional segmentations of the tomograms. We also gratefully acknowledge funding of this project by the German Research Foundation (Deutsche Forschungsgemeinschaft) under contract Ge 841/26, the National Institutes of Health (NIH) under grant R35GM119023, the Wadsworth Center 3D-EM Facility and travel support by the Karlsruhe House of Young Scientists (KHYS of the Karlsruhe Institute of Technology, KIT). S.H. acknowledges funding by the German Research Foundation (HE 7675/1-1).

Supplementary materials

Supplementary material associated with this article can be found, in the online version, at doi:10.1016/j.ultramic.2020.113086.

References

[1] O. Scherzer, The Theoretical Resolution Limit of the Electron Microscope, J. Appl. Phys. 20 (1949) 20–29, https://doi.org/10.1063/1.1698233.
[2] R.M. Glaeser, Invited Review Article: Methods for imaging weak-phase objects in electron microscopy, Rev. Sci. Instrum. 84 (2013) 111101, , https://doi.org/10.1063/1.4830355.
[3] F. Zernike, Phase contrast, a new method for the microscopic observation of transparent objects, Physica 9 (1942) 686–698, https://doi.org/10.1016/S0031-8914(42)80035-X.
[4] H. Boersch, Über die Kontraste von Atomen im Elektronenmikroskop, Z. Naturforsch. 2a (1947) 615–633.
[5] R. Danev, K. Nagayama, Transmission electron microscopy with Zernike phase plate, Ultramicroscopy 88 (2001) 243–252, https://doi.org/10.1016/S0304-3991(01)00088-2.
[6] D. Willasch, High-resolution electron microscopy with profiled phase plates, Optik 44 (1975) 17–36.
[7] R. Danev, R.M. Glaeser, K. Nagayama, Practical factors affecting the performance of a thin-film phase plate for transmission electron microscopy, Ultramicroscopy 109 (2009) 312–325, https://doi.org/10.1016/j.ultramic.2008.12.006.
[8] M. Malac, M. Beleggia, M. Kawasaki, P. Li, R.F. Egerton, Convenient contrast enhancement by a hole-free phase plate, Ultramicroscopy 118 (2012) 77–89, https://doi.org/10.1016/j.ultramic.2012.02.004.
[9] R. Danev, B. Buijsse, M. Khoshouei, J.M. Plitzko, W. Baumeister, Volta potential phase plate for in-focus phase contrast transmission electron microscopy, Proc. Natl. Acad. Sci. U. S. A. 111 (2014) 15635–15640, https://doi.org/10.1073/pnas.1418377111.
[10] S. Hettler, E. Kano, M. Dries, D. Gerthsen, L. Pfaffmann, M. Bruns, M. Beleggia, M. Malac, Charging of carbon thin films in scanning and phase-plate transmission electron microscopy, Ultramicroscopy 184 (2018) 252–266, https://doi.org/10.1016/j.ultramic.2017.09.009.
[11] S. Hettler, J. Onoda, R. Wolkow, J. Pitters, M. Malac, Charging of electron beam irradiated amorphous carbon thin films at liquid nitrogen temperature, Ultramicroscopy 196 (2019) 161–166, https://doi.org/10.1016/j.ultramic.2018.10.010.
[12] R. Pretzsch, M. Dries, S. Hettler, M. Spiecker, M. Obermair, D. Gerthsen, Investigation of hole-free phase plate performance in transmission electron microscopy under different operation conditions by experiments and simulations, Adv. Struct. Chem. Imag. 5 (2019) 20, https://doi.org/10.1186/s40679-019-0067-z.
[13] M. Malac, S. Hettler, M. Hayashida, M. Kawasaki, Y. Konyuba, Y. Okura, H. Iijima, I. Ishikawa, M. Beleggia, Computer simulations analysis for determining the polarity of charge generated by high energy electron irradiation of a thin film, Micron 100 (2017) 10–22, https://doi.org/10.1016/j.micron.2017.03.015.
[14] R. Danev, D. Tegunov, W. Baumeister, Using the Volta phase plate with defocus for cryo-EM single particle analysis, eLife 6 (2017) e23006, https://doi.org/10.7554/eLife.23006.
[15] R. Danev, W. Baumeister, Cryo-EM single particle analysis with the Volta phase plate, eLife 5 (2016) e13046, https://doi.org/10.7554/eLife.13046.
[16] M. Khoshouei, M. Radjainia, W. Baumeister, R. Danev, Cryo-EM structure of haemoglobin at 3.2 Å determined with the Volta phase plate, Nat. Comms. 8 (2017) 16099, https://doi.org/10.1038/ncomms16099.
[17] Y.-L. Liang, M. Khoshouei, M. Radjainia, Y. Zhang, A. Glukhova, J. Tarrasch, D.M. Thal, S.G.B. Furness, G. Christopoulos, T. Coudrat, R. Danev, W. Baumeister, L.J. Miller, A. Christopoulos, B.K. Kobilka, D. Wootten, G. Skiniotis, P.M. Sexton, Phase-plate cryo-EM structure of a class B GPCR-G-protein complex, Nature 546 (2017) 118–123, https://doi.org/10.1038/nature22327.
[18] S. Asano, Y. Fukuda, F. Beck, A. Aufderheide, F. Förster, R. Danev, W. Baumeister, A molecular census of 26S proteasomes in intact neurons, Science 347 (2015) 439–442, https://doi.org/10.1126/science.1261197.
[19] J. Mahamid, S. Pfeffer, M. Schaffer, E. Villa, R. Danev, L.K. Cuellar, F. Förster, A.A. Hyman, J.M. Plitzko, W. Baumeister, Visualizing the molecular sociology at the HeLa cell nuclear periphery, Science 351 (2016) 969–972, https://doi.org/10.1126/science.aad8857.
[20] A. Kotani, K. Harada, M. Malac, M. Salomons, M. Hayashida, S. Mori, Observation of FeGe skyrmions by electron phase microscopy with hole-free phase plate, AIP Adv. 8 (2018) 55216, https://doi.org/10.1063/1.5028398.
[21] Y. Fukuda, U. Laugks, V. Lučić, W. Baumeister, R. Danev, Electron cryotomography of vitrified cells with a Volta phase plate, J. Struct. Biol. 190 (2015) 143–154,

https://doi.org/10.1016/j.jsb.2015.03.004.
[22] K. Schultheiss, J. Zach, B. Gamm, M. Dries, N. Frindt, R.R. Schröder, D. Gerthsen, New Electrostatic Phase Plate for Phase-Contrast Transmission Electron Microscopy and Its Application for Wave-Function Reconstruction, Microsc. Microanal. 16 (2010) 785–794, https://doi.org/10.1017/S1431927610093803.
[23] N. Frindt, M. Oster, S. Hettler, B. Gamm, L. Dieterle, W. Kowalsky, D. Gerthsen, R.R. Schröder, In-Focus Electrostatic Zach Phase Plate Imaging for Transmission Electron Microscopy with Tunable Phase Contrast of Frozen Hydrated Biological Samples, Microsc. Microanal. 20 (2014) 175–183, https://doi.org/10.1017/S1431927613013901.
[24] S. Hettler, M. Dries, J. Zeelen, M. Oster, R.R. Schröder, D. Gerthsen, High-resolution transmission electron microscopy with an electrostatic Zach phase plate, New J. Phys. 18 (2016) 53005, https://doi.org/10.1088/1367-2630/18/5/053005.
[25] M.L. Yap, M.G. Rossmann, Structure and function of bacteriophage T4, Future Microbiol. 9 (2014) 1319–1327, https://doi.org/10.2217/fmb.14.91.
[26] P.G. Leiman, S. Kanamaru, V.V. Mesyanzhinov, F. Arisaka, M.G. Rossmann, Structure and morphogenesis of bacteriophage T4, Cell. Mol. Life Sci. 60 (2003) 2356–2370, https://doi.org/10.1007/s00018-003-3072-1.
[27] S. Hettler, B. Gamm, M. Dries, N. Frindt, R.R. Schröder, D. Gerthsen, Improving Fabrication and Application of Zach Phase Plates for Phase-Contrast Transmission Electron Microscopy, Microsc. Microanal. 18 (2012) 1010–1015, https://doi.org/10.1017/S1431927612001560.
[28] M. Marko, C. Hsieh, E. Leith, D. Mastronarde, S. Motoki, Practical Experience with Hole-Free Phase Plates for Cryo Electron Microscopy, Microsc. Microanal. 22 (2016) 1316–1328, https://doi.org/10.1017/S143192761601196X.
[29] H. Minoda, T. Okabe, H. Iijima, Contrast enhancement in the phase plate transmission electron microscopy using an objective lens with a long focal length, J. Electron Microsc. 60 (2011) 337–343, https://doi.org/10.1093/jmicro/dfr067.
[30] D.N. Mastronarde, Automated electron microscope tomography using robust prediction of specimen movements, J. Struct. Biol. 152 (2005) 36–51, https://doi.org/10.1016/j.jsb.2005.07.007.
[31] R.F. Thompson, M. Walker, C.A. Siebert, S.P. Muench, N.A. Ranson, An introduction to sample preparation and imaging by cryo-electron microscopy for structural biology, Methods 100 (2016) 3–15, https://doi.org/10.1016/j.ymeth.2016.02.017.
[32] S. Hettler, J. Wagner, M. Dries, M. Oster, C. Wacker, R.R. Schröder, D. Gerthsen, On the role of inelastic scattering in phase-plate transmission electron microscopy, Ultramicroscopy 155 (2015) 27–41, https://doi.org/10.1016/j.ultramic.2015.04.001.
[33] J. Barthel, A. Thust, Aberration measurement in HRTEM: Implementation and diagnostic use of numerical procedures for the highly precise recognition of diffractogram patterns, Ultramicroscopy 111 (2010) 27–46, https://doi.org/10.1016/j.ultramic.2010.09.007.
[34] J.R. Kremer, D.N. Mastronarde, J.R. McIntosh, Computer Visualization of Three-Dimensional Image Data Using IMOD, J. Struct. Biol. 116 (1996) 71–76, https://doi.org/10.1006/jsbi.1996.0013.
[35] J. Schindelin, I. Arganda-Carreras, E. Frise, V. Kaynig, M. Longair, T. Pietzsch, S. Preibisch, C. Rueden, S. Saalfeld, B. Schmid, J.-.Y. Tinevez, D.J. White, V. Hartenstein, K. Eliceiri, P. Tomancak, A. Cardona, Fiji: an open-source platform for biological-image analysis, Nat. Methods 9 (2012) 676–682, https://doi.org/10.1038/nmeth.2019.
[36] A.H. Tavabi, M. Beleggia, V. Migunov, A. Savenko, O. Öktem, R.E. Dunin-Borkowski, G. Pozzi, Tunable Ampere phase plate for low dose imaging of biomolecular complexes, Sci. Rep. 8 (2018) 5592, https://doi.org/10.1038/s41598-018-23100-3.
[37] A. Harscher, H. Lichte, Inelastic Mean Free Path and Mean Inner Potential of Carbon Foil and Vitirfied Ice measured with Electron Holography, Electron Microscopy 1 (1998) 553–554.
[38] W.M.J. Coene, A. Thust, M. Op de Beeck, D. Van Dyck, Maximum-likelihood method for focus-variation image reconstruction in high resolution transmission electron microscopy, Ultramicroscopy 64 (1996) 109–135, https://doi.org/10.1016/0304-3991(96)00010-1.
[39] E. Majorovits, R.R. Schröder, EP1476890B1 (2014).
[40] E. Majorovits, B. Barton, K. Schultheiß, F. Pérez-Willard, D. Gerthsen, R.R. Schröder, Optimizing phase contrast in transmission electron microscopy with an electrostatic (Boersch) phase plate, Ultramicroscopy 107 (2007) 213–226, https://doi.org/10.1016/j.ultramic.2006.07.006.
[41] D. Tschumperlé, R. Deriche, Vector-valued image regularization with PDEs: a common framework for different applications, IEEE Trans. Pattern Anal. Mach. Intell 27 (2005) 506–517, https://doi.org/10.1109/TPAMI.2005.87.